Materials Science & Engineering A 613 (2014) 201–208

Contents lists available at ScienceDirect

Materials Science & Engineering A

journal homepage: www.elsevier.com/locate/msea

Alloying and the micromechanics of Co–Al–W–X quaternary alloys

Hui-Yu Yan [a], James Coakley [a], Vassili A. Vorontsov [a], Nicholas G. Jones [b], Howard J. Stone [b], David Dye [a,*]

[a] Department of Materials, Royal School of Mines, Imperial College London, Prince Consort Road, London SW7 2BP, UK
[b] Department of Materials Science and Metallurgy, University of Cambridge, 27 Charles Babbage Road, Cambridge CB3 0FS, UK

ARTICLE INFO

Article history:
Received 18 March 2014
Accepted 13 May 2014
Available online 22 May 2014

Keywords:
Co–Al–W superalloys
Synchrotron X-ray diffraction
Neutron scattering
Elastic behaviour

ABSTRACT

The lattice misfit and diffraction elastic constants in hot rolled polycrystalline Co–7Al–5W–2Ta and Co–6Al–6W–2Ti (at.%) are measured using neutron and synchrotron X-ray diffraction. The misfit in the two alloys was found to be +0.67 and +0.59%, using neutron diffraction at HRPD. The misfit was found to increase with temperature, as in Ni superalloys. This implies that the amount of coherency strengthening increases with temperature. The diffraction elastic constants measured show that the γ' phase is less stiff than the γ matrix in all orientations, which means that load shedding will occur to the γ phase.

1. Introduction

Ni base superalloys play an important role in the modern aircraft engine, comprising approximately 40–50% of its weight [1]. The principal strengthening mechanisms are dependent on the presence of coherent $L1_2$-γ' precipitates (Ni_3Al), in an FCC solid solution, A1-γ matrix. Ni base superalloys are chosen for the hottest sections of gas turbines, due to the γ' precipitates showing an anomalous increase in strength with increasing temperature. Therefore, the alloys exhibit superior creep and fatigue properties at elevated temperatures [2–4].

The increase in the number of aircraft worldwide and high oil prices makes fuel economy the biggest challenge for the aircraft industry [5]. Increases in temperature allow for improvements in cycle efficiency, and this design criterion is a potent driver for the development of new alloy systems to replace Ni base superalloys. These alloys are now quite mature, with successive generations showing limited improvement in temperature capability.

In 2006, Sato et al. [6] discovered a new $L1_2$ γ' phase, $Co_3(Al,W)$, in the Co–Al–W ternary system which coexists with the FCC Co matrix. The lattice misfit between the γ and γ' phases is ~0.53%, which allows cuboidal $Co_3(Al,W)$ phase precipitates to exist in the γ matrix with a high degree of coherency. The microstructure of these Co–Al–W base alloys is therefore quite similar to Ni base superalloys.

Co–Al–W base alloys exhibit the flow stress anomaly [7–10] with limited or no decrease in the flow stress at temperatures up to 600 °C. The addition of elements such as Ti, Ta and Ir to the base alloy increases the γ' solvus temperature and improves strength. Moreover, the addition of boron has a remarkable effect by providing grain boundary strengthening. Further investigation [11–14] showed that $Co_3(Al,W)$ is metastable at 1000 °C, decomposing into either γ, CoAl and Co_7W_6 or γ, Co_7W_6 and Co_3W. It was also shown that for long aging time at 900 °C , discontinuously coarsened lamellar colonies (regions of lamellar orientation) form at the γ grain boundaries. Four phases were found in the colonies: γ, γ', CoAl and Co_3W.

Knowledge of the elastic properties of both γ and γ' phases is critical for a fundamental understanding of the mechanical behaviour of the Co–Al–W base alloys. Lattice misfit (δ) is another very important microstructural parameter that determines the mechanical properties in the superalloys, defined as $\delta = 2(a_{\gamma'} - a_{\gamma})/(a_{\gamma} + a_{\gamma'})$ [2]. Positive lattice misfit has been observed at both room temperature and elevated temperature during high-energy X-ray diffraction experiments [6,15]. Positive misfit would be expected to lead to directional coarsening (rafting) parallel to the applied tensile stress [16]. Microstructural stability is favoured by small lattice misfit, i.e. low surface energies that provide the driving force for coarsening. The magnitude of the lattice misfit varies strongly with temperature in Ni base superalloys [17,18]. The reliable prediction of these properties in multicomponent alloys is difficult and, given the importance of lattice misfit in determining mechanical properties, it is necessary to study this dependence over a range of temperatures up to the γ' solvus in the Co–Al–W system.

It is also valuable to understand the load partitioning between the γ and γ' phases that arises due to stiffness differences. Load partitioning will affect the stresses that evolve in the two phases during creep, both during particle shearing and non-shearing

* Corresponding author. Tel.: +44 797 707 6141.
E-mail address: ddye@ic.ac.uk (D. Dye).

http://dx.doi.org/10.1016/j.msea.2014.05.044

regimes. It will also affect the driving force for rafting in the very high temperature creep regime. Recently, both experimental and theoretical calculations to determine the moduli of the two phases at cryogenic temperatures have been performed [20–23]. Density functional theory calculations suggest that the shear modulus G (at 0 K) of the γ' is rather large, which would increase the resistance to dislocation motion and hence improve the strength. Furthermore, the intrinsic ductility of the intermetallic is determined by the ratio G/B, where B is the bulk modulus. The calculated data suggest that the γ' phase behaves in a brittle manner. However, the experimental data for a polycrystal at 5 K suggest that $G/B < 0.5$, which would suggest that the γ' is intrinsically ductile. It has been shown that in Ni base superalloys the elastic moduli are temperature dependent. To the authors' knowledge, no data has been published about the γ and γ' moduli for these Co–Al–W base alloys at both room and elevated temperatures.

In this work, synchrotron and neutron diffraction measurements have been performed to study the micromechanics of Co–Al–W–X quaternary alloys. The variation of the lattice misfit values and the variation of diffraction elastic constants (DECs) over a range of temperatures have been measured and are discussed. A comparison is made between the different diffraction techniques.

2. Experimental description

2.1. Alloy processing route

50 g finger-shaped polycrystalline ingots of different compositions were produced by vacuum arc melting in a back-filled argon atmosphere. The nominal compositions and the actual compositions obtained are presented in Table 1. The ingots were solution heat-treated at 1300 °C for 24 h. Subsequently, the ingots were encapsulated in rectilinear mild steel cans with Ti powder packing. The first batch of alloys produced was super solvus hot rolled at 1150 °C to a thickness of ~3 mm, and the second batch of alloys produced was hot rolled to ~6 mm. Differential Scanning Calorimetry (DSC) was performed to obtain cooling curves for the alloys, from which the solvus temperatures were determined, presented in Table 1. The alloys were aged at 80–100 °C below the solvus temperature. For all the heat treatments, the alloys were sealed in quartz tubes, which were back-filled with argon after evacuation and were furnace cooled.

Alloy compositions were determined by Inductively Coupled Plasma-Optical Emission Spectroscopy (ICP-OES) at Incotest, Hereford, UK.

2.2. Microscopy

Microstructural examination was performed using a LEO 1525 Field Emission Gun Scanning Electron Microscope (FEG-SEM) in secondary electron imagining mode. The samples were ground, polished and etched using a Spar etchant solution [24,25] (100 ml of distilled water, 100 ml of 32% HCl, 10 ml of 65% HNO_3 and 0.3 ml of Spar etchant, with 1-methoxy-2-propanol as the main constituent) for 3 s.

An FEI TITAN 80/300 Transmission Electron Microscope (TEM) was used to determine the lattice misfit value of the 2Ta alloy, in order to provide a comparison with the values measured by neutron diffraction and Synchrotron X-Ray Diffraction (SXRD). As the alloy is magnetic, examination of a randomly orientated grain is rather complicated in TEM [24]. For this reason, TEM specimens were prepared by FIB-milling (Helios NanoLab-DualBeam), normal to a ⟨100⟩ direction.

2.3. HRPD experiment to determine lattice misfit

Neutron diffraction experiments were conducted on the HRPD (High Resolution Powder Diffraction) beamline at the ISIS facility, Didcot, Oxon, UK. The aim of this experiment was to determine the evolution of lattice misfit with temperature. A schematic representation of the experimental setup is shown in Fig. 1a. The HRPD instrument is a high resolution, long flight path, Time-of-Flight (TOF) spallation neutron diffraction beamline with detector banks at 168°, ±90° and 30°. The 168° bank is a backscattering detector and was employed in this study to obtain maximum d-spacing resolution. It can cover a wide d-spacing range with a resolution of $\Delta d/d \sim 4 \times 10^{-4}$ [26]. Specimens were produced from the second batch (~6 mm thick) and machined into 40 mm long and 3 mm wide strips by Electrical Discharge Machining (EDM). Several pieces of each alloy were packed inside a neutron-transparent vanadium can and placed in an infra-red vacuum furnace. Room temperature and elevated temperature (with 100 °C increments) neutron diffraction data were collected for each alloy. Typical neutron count times were ~20 min for each measurement.

2.4. SXRD experiment to determine lattice misfit and DECs

SXRD measurements were made using the I12 beamline at the Diamond synchrotron, Didcot, Oxon, UK. Tensile specimens with a gauge section of 19 × 1.5 × 2 mm were prepared from the batch 1 alloys using EDM with the gauge length parallel to the rolling direction. The aim of this experiment was to determine the lattice misfit and DECs at room temperature and elevated temperatures. The experimental set-up is shown in Fig. 1b. The dog-bone specimens were tested using a Zwick-Roell 5 kN tensile test rig in the beamline. An infrared furnace was mounted onto the load frame. Specimens were loaded from 0 MPa to 270 MPa under displacement control at a strain rate of $10^{-4}\,s^{-1}$. Room temperature diffraction data were recorded during loading with an exposure time of 1 s. Following unloading, the temperature was ramped to 100 °C, isothermally held, with the loading and diffraction data measurement process repeated. Following the 100 °C measurement the temperature was increased in 50 °C increments, with the same loading and data measurement procedure. The process was performed until temperatures were reached just below the solvus temperature of each alloy, Table 1. A 79 keV (λ=0.15675 Å), 500 × 500 μm monochromated X-ray beam was used during the

Table 1
Measured compositions (ICP-OES), γ' solvus temperature and secondary γ' area fractions (A_f) of the alloys studied. The subscript "#2" denotes the second batch alloys. The alloys were furnace cooled after sub-solvus ageing.

Alloy (at.%)	Abbreviation	Composition (at.%)			Ageing °C	Solvus °C	$A_{f(\gamma')}$ %
		Al	W	others			
86Co–7Al–5W–2Ta	2Ta	9.9	4.8	1.8 Ta	900 °C / 100 h	992	42
86Co–7Al–5W–2Ta	$2Ta_{\#2}$	10.1	4.9	1.7 Ta	900 °C / 100 h	982	–
86Co–6Al–6W–2Ti	2Ti	6.4	6.0	2.2 Ti	830 °C / 200 h	919	58
86Co–6Al–6W–2Ti	$2Ti_{\#2}$	6.5	6.0	2.3 Ti	830 °C / 200 h	921	–

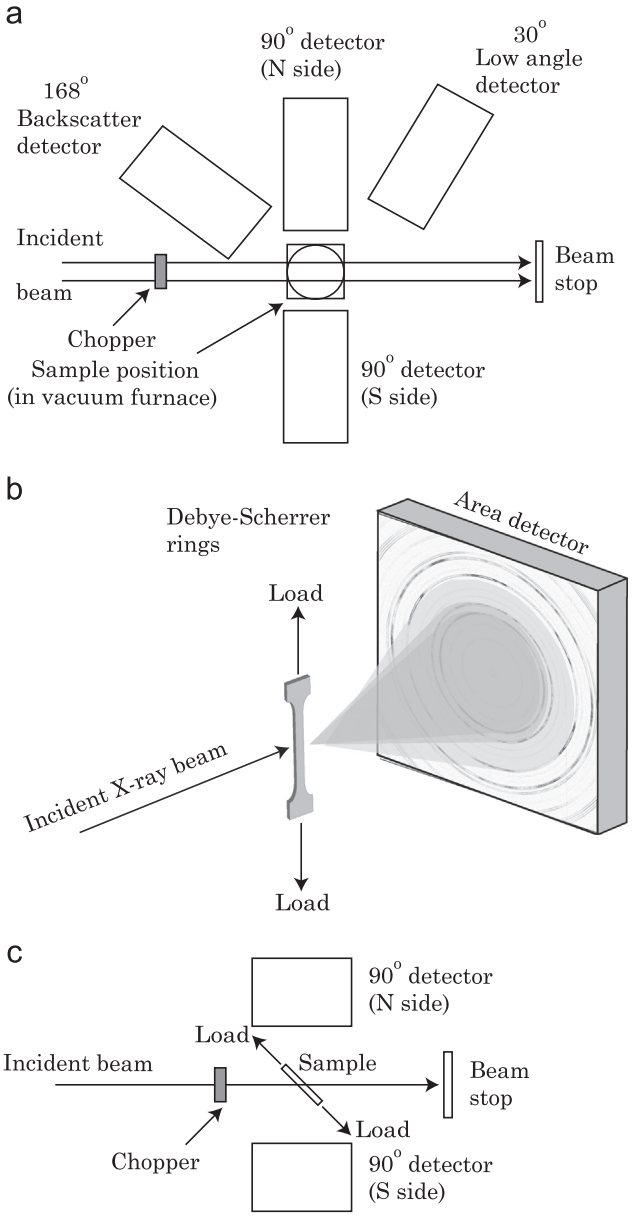

Fig. 1. Schematic depictions of (a) the HRPD detector configuration in plan view; (b) the in situ SXRD experiment at I12; (c) the Vulcan neutron diffractometer at SNS. Figure adapted from [24].

tensile loading and the diffraction data were recorded using a Thales Pixium 2D area detector, 1319 mm from the specimen, in order to obtain full Debye–Scherrer diffraction rings. The rings were integrated to provide intensity-2θ diffraction spectra using the Fit2D software package [27].

2.5. Measuring lattice misfit and DECs at the Vulcan diffractometer

Vulcan, the medium resolution TOF neutron diffractometer at the Spallation Neutron Source (SNS) at Oak Ridge National Laboratory (ORNL), TN, USA, was also used to study the batch 2 alloys, Fig. 1c. Dog-bone specimens with gauge dimensions of $19 \times 1.5 \times 3$ mm were mounted horizontally in a stress rig at 45° to the incident beam. The gauge volume of the sample was heated using electromagnetic induction. The detectors are located at $\pm 90°$. The aim of this experiment was to determine the evolution of the lattice misfit and DECs with temperature. To determine DECs, it is desirable to use the widest stress range possible while avoiding yielding. Therefore the stresses used to measure the DEC's were reduced as the temperature was increased, Table 2. For the 2Ti alloy, a similar procedure was used. Count times at each stress level were 10 min.

Table 2
An example of the experimental loading procedure used at Vulcan (2Ta alloy). The stress was incremented gradually as indicated, with the stress range being reduced as the temperature was increased. The specimen failed at 600 °C/300 MPa.

30 °C, 150 °C Load (MPa)	300 °C, 400 °C Load (MPa)	500 °C, 600 °C Load (MPa)
20	20	20
100	90	50
200	160	100
300	230	150
400	300	200
500	370	250
600	450	300

3. Results and discussion

3.1. Initial characterisation

The alloy compositions, solvus temperatures and secondary γ' fractions are listed in Table 1. The achieved compositions were within 0.3 at.%, except for Al. The area fractions of γ' phase presented in Table 1 were obtained by thresholding SEM images in the ImageJ software package to produce a binary γ and γ' image. Three SEM images, e.g. Fig. 2, were analysed from different grains such that the area fraction is representative of the alloy and it is assumed that the area fraction of the γ' phase is equivalent to the γ' volume fraction. However, this approach only measures the secondary γ' fraction, and ignores the fine (<10 nm) tertiary γ' present in the 2Ta alloy.

The solvus temperatures for the two batches of alloys are quite similar, within 10 °C. For this reason, these two batches were selected for detailed comparison. As previously observed by other workers, Ta additions raise the solvus temperature dramatically [7,8,10,28].

The 2Ta alloy possesses a cuboidal γ' morphology, with an average secondary γ' size after ageing of 200 nm. The secondary γ' area fraction was 42%. It should be noted that the total γ' area fraction is greater than 42%, when one accounts for the tertiary γ', observable in the micrograph. The fraction and size distribution of the tertiary γ' will depend on the ageing temperature and the form of the solvus curve with temperature. This means that, although both alloys were aged approximately 90 °C below the solvus, the relative γ' fractions cannot be inferred from the secondary γ' contents alone.

The Ti-containing alloys had a solvus temperature ~70 °C lower than the Ta alloys. Therefore, alloying the Co–Al–W base alloy with Ti has a smaller effect on the solvus temperature than alloying with Ta. The secondary γ' area fraction for the 2Ti alloy is slightly greater than in the 2Ta alloy, with the secondary γ' size being ~80 nm. The longer ageing time used may also have had an influence on the amount of secondary γ' observed.

3.2. Analysis of X-ray and neutron scattering data to obtain lattice misfit values

Si powder standards were used to calibrate the HRPD and I12 instruments. The intensity-2θ profiles (SXRD data) and the intensity-TOF profiles (HRPD neutron diffraction data) were fitted using Rietveld refinement [29,30] with the General Structure

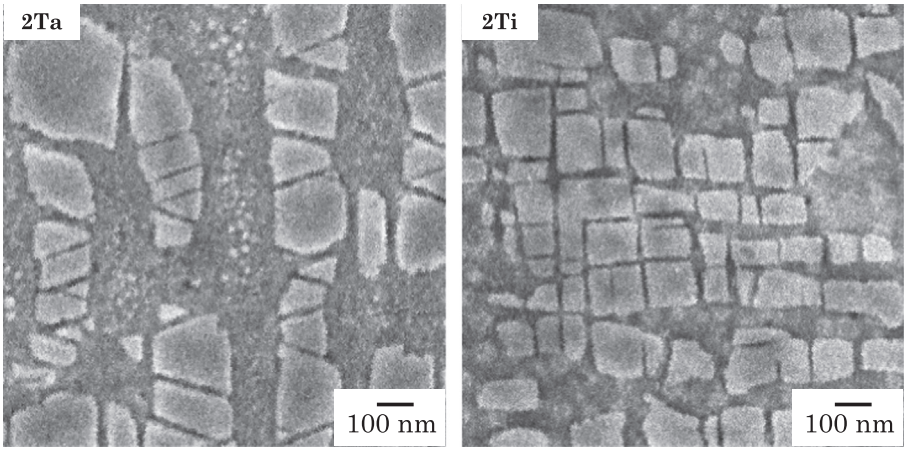

Fig. 2. Microstructure of the base alloy; microstructures obtained for the first batch of alloys after the ageing heat treatment.

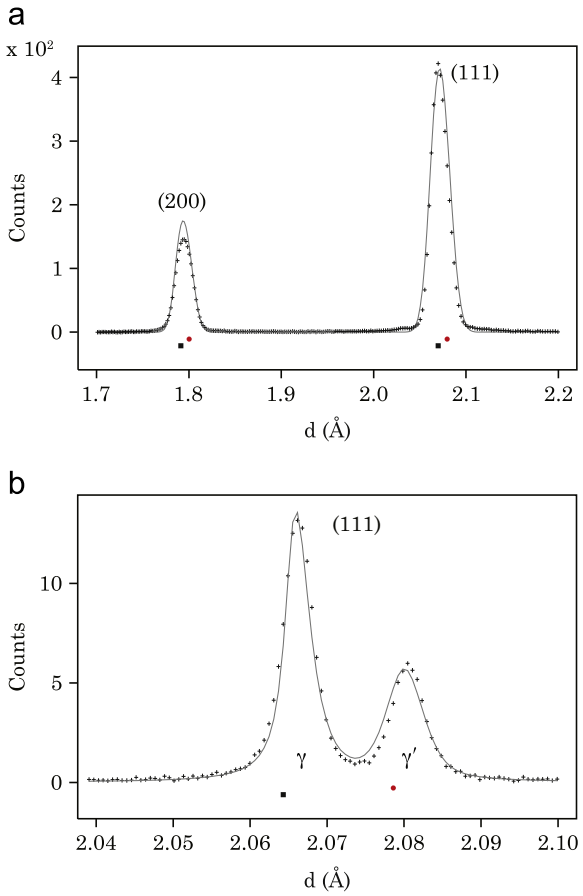

Fig. 3. Examples of the fitted diffraction spectra obtained from the 2Ta alloy at RT and zero load (a) by SXRD (I12, Diamond), (b) by neutron diffraction (HRPD). Red circle and black square markers correspond to γ' and γ peaks, respectively. (For interpretation of the references to colour in this figure caption, the reader is referred to the web version of this paper.)

Analysis System (GSAS) [31] software, in order to obtain the initial unstrained lattice parameters of each phase. In this fitting routine, it was assumed that there was only Co in the FCC γ matrix, and the alloying elements partitioned to the $Co_3(Al,W)$ γ' $L1_2$ phase. Fig. 3 shows the GSAS-fitted diffraction spectra obtained for the 2Ta alloy at room temperature and zero load (a) at I12 (SXRD), (b) at HRPD (neutrons).

The γ' is an ordered superlattice structure of the γ. Therefore, for peaks with {*hkl*} all odd or all even, the observed peaks are doublets due to scattering from both the γ and γ' phases. If {*hkl*} indices are mixed, the γ phase is systematically absent, but the superlattice reflection may still occur from the $L1_2$ γ' phase. Therefore, the {100}, {110}, {210} and {211} peaks are only from the γ' whilst the {111}, {200} and {220} are doublet γ and γ' peaks.

Two distinct peaks are observed for the {111} using HRPD (Fig. 3b), whereas the γ and γ' peaks are overlapped in the SXRD spectra from I12 (Fig. 3a). This can be explained by the difference in resolution of the two instruments. Because the lattice parameters of the two phases are very close, the peaks may not be satisfactorily resolved if the resolution is poor. The backscatter bank in HRPD is designed to achieve $\Delta d/d \sim 0.05\%$, which is the highest resolution neutron diffractometer in the world. The resolution for SXRD at I12 is $\sim \Delta d/d \sim 0.5\%$. In the present case, the HRPD peak width is limited by the defect state associated with using non-powder samples and the presence of intermetallic phases, and the resolution is only around 0.2%. This still allows the two peaks to be resolved, with a mismatch strain (misfit) of around 0.7%.

In contrast, the two peaks cannot be resolved at I12 and the reliance in the Rietveld refinement is placed on the superlattice peaks instead. Thus, the {100} γ' peak provides the primary information to locate the {200} γ' from the composite γ/γ' reflection, allowing the refinement to then isolate the {200} γ lattice parameter. When performed manually, this reduces to the technique described by Stone et al. [32].

3.3. Analysis of X-ray and neutron scattering data to obtain DECs

Separate Voigt single and doublet peak fitting routines were employed in order to determine the lattice strains of each phase in each plane for the synchrotron data, using the Wavemetrics Igor Pro program, Fig. 4. This allowed the determination of the (plane-specific) diffraction elastic constants. The {200} and {220} composite doublet peaks were fitted in a similar method to the method described by Coakley et al. [17,33,18]. It was assumed that (i) both the γ and γ' have the same instrumental peak widths, (ii) the shape of the Voigt function is the same in both γ and γ' peaks, (iii) the positions of the {200} and {220} γ' peaks are fixed from the position of the {100} and {110} γ' peaks respectively, and (iv) the intensity ratio $I^{\gamma}/I^{\gamma'}$ of each γ and γ' phase in the {200} and {220} doublet peaks was defined from $V_f^{\gamma}/V_f^{\gamma'}$. The $V_f^{\gamma'}$ were estimated from SEM, Table 1. It has previously been determined that this approach performs just as well as structure factor-based calculations [32]. For the 2Ta alloy, the intensity ratio was defined from the secondary γ' precipitate area fraction. The 2Ta data was also

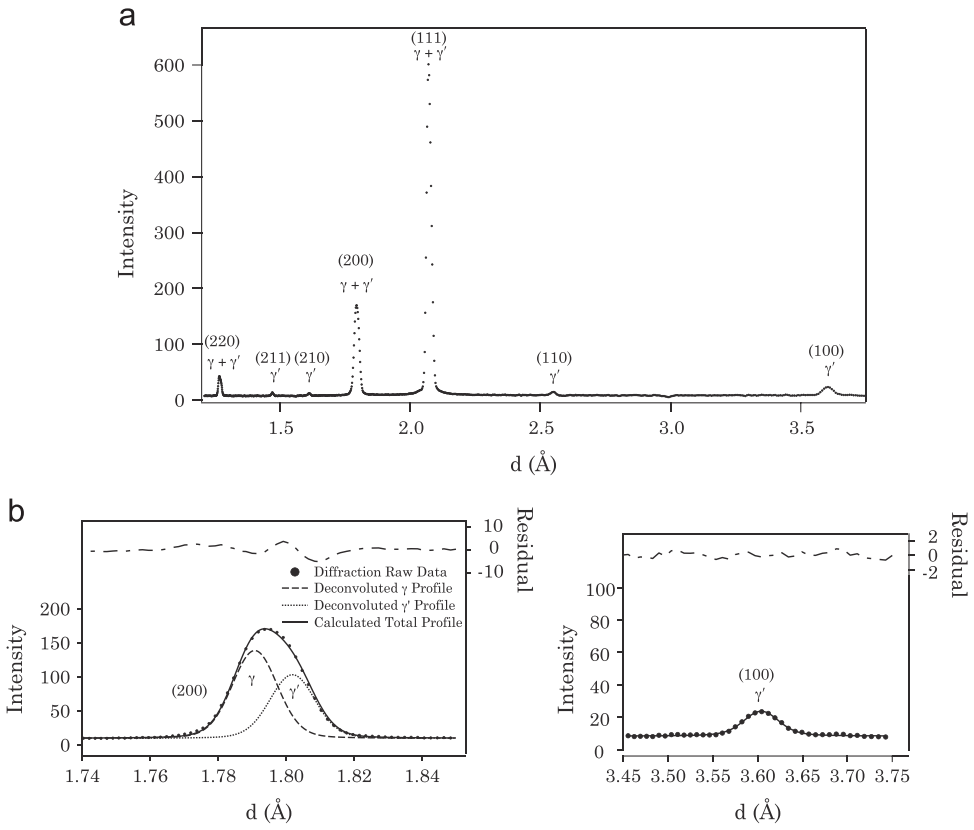

Fig. 4. (a) Diffraction spectrum obtained by synchrotron diffraction for 2Ta at RT and zero stress. (b) Example of the single peak and double peak fitting routines employed during the data analysis, with an intensity ratio $I'/I'' = 1.38$.

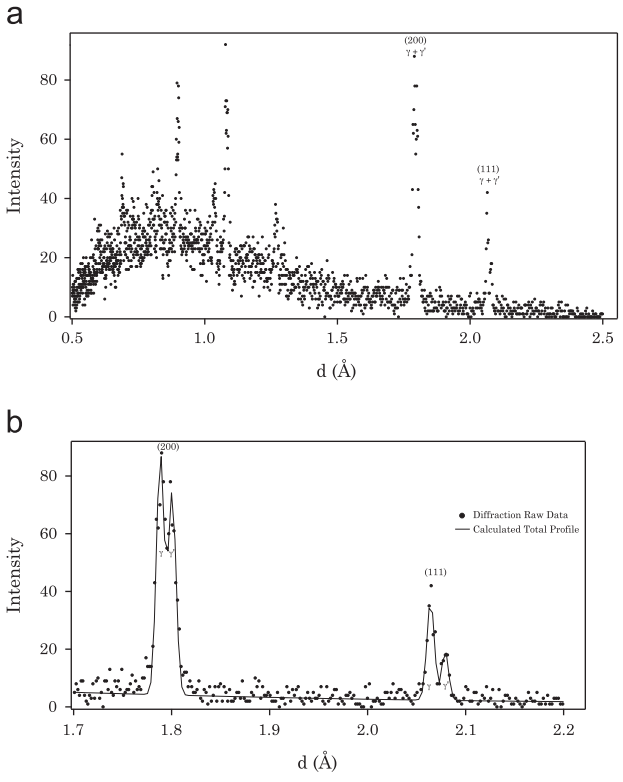

Fig. 5. (a) Vulcan TOF neutron diffraction spectrum obtained for 2Ta alloy at room temperature and zero stress. (b) Example of (111) and (200) double peak fitting routine used in the Wavemetrics program Igor Pro.

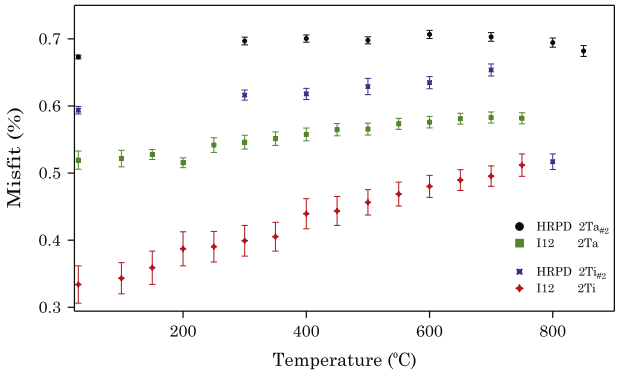

Fig. 6. Evolution of lattice misfit with temperature for the 2Ta alloys measured by both techniques. The uncertainties estimated from the Rietveld refinement are shown.

fitted with a higher volume fraction (48%) to account for the tertiary γ' precipitates, and the lattice parameters were found to be insensitive to small changes in volume fraction.

Fig. 5a shows the TOF neutron diffraction spectra for the 2Ta alloy at room temperature and zero load condition. The resolution of Vulcan is lower than that of HRPD, with $r\,\Delta d/d \simeq 0.25\%$, but it was still possible to observe distinct γ and γ' peaks for the {111} and {200}, Fig. 5b. As with the I12 data, Wavemetrics Igor Pro was used to fit the doublet peaks, but without the need to refer to the superlattice reflections. However, the intensity ratio and the width were fixed for each phase.

3.4. Lattice misfit and its dependence on temperature

Fig. 6 shows the lattice misfit and its evolution with temperature for the 2Ta and 2Ti alloys in the unloaded condition, from the Rietveld-refined neutron HRPD data and the I12 data. It should be noted that the samples were from different alloy melts, Table 1. Both the HRPD and I12 show that the lattice parameter for γ' is always greater than that for γ, that is, the misfit is positive and increases with temperature. In contrast, commercial Ni base superalloys such as CMSX-4 have a negative misfit of around -0.2%, which also increases with temperature, becoming nearly zero at service temperatures [34,35,18].

In addition to the importance of the sign and magnitude of misfit for rafting and coarsening, the misfit is also the determinant of the amount of coherency strengthening. Commercial Ni base superalloys derive much of their strength from anti-phase boundary strengthening; that is, the requirement for dislocations shearing the γ' to do so in groups, forming dislocation ribbons [36,37]. Because Ni base superalloys have been engineered to minimise coarsening and hence misfit, the contribution from coherency strengthening is often quite low at temperature. In contrast, superalloys exploiting the $Co_3(Al,W)$ phase should suffer minimal coarsening because of the low solubility and diffusivity of W in the matrix γ phase. Hence, significant contributions from the large (up to 0.7%) misfit values measured here might be found.

The I12 data for the 2Ti alloy is perhaps the clearest. It shows that the misfit increases from $\sim$0.33% at RT to 0.51% at 750 °C, indicating a difference in thermal expansion coefficient between the two phases of $2\times10^{-6}\,K^{-1}$. The I12 data for the 2Ta alloy shows a much smaller thermal expansion coefficient differential between the two phases, of around $0.5\times10^{-6}\,K^{-1}$. In addition, both the neutron and X-ray results indicate that the 2Ta alloy has a higher misfit, by 0.1–0.2%.

This can be rationalised by considering the atomic radii of the constituent elements. Metallic Al and W have very similar atomic radii, 1.43 and 1.37 Å, respectively. Both Co and Ni have atomic radii of 1.25 Å [38]. Appealing to the Hume-Rothery rules [39], it is therefore expected both that Ni–Al solutions would order to form Ni_3Al and that Al and W could form a sublattice together in the newly discovered $Co_3(Al,W)$ phase. Ti has an atomic radius of 1.45 Å and Ta, 1.43 Å. Therefore, it is expected that both Ti and Ta will increase the γ' lattice parameter and misfit and that both are strong γ' formers. We hypothesise that Ta segregates even more strongly to the γ' phase than Ti, which is consistent with its effect on the γ' fraction [40,41], presumably because of its higher valency, and this then provides a rationale for why Ta increases the misfit more than Ti.

As the temperature increases beyond 700 °C, the HRPD data suggests that the misfit begins to decrease in both alloys, and by a greater amount in the 2Ti alloy than in 2Ta. This approximately coincides with the temperature at which dissolution of the γ' begins, which is presumably a related phenomenon.

Disappointingly, the two techniques give misfit values that are quite different, by around 0.15% for the 2Ta alloy and over 0.2% for the 2Ti alloy. It should be noted that different alloy batches were used and so some of the discrepancy may be due to melt-to-melt variability. The HRPD experiment (i) used a diffractometer with higher resolution which was good enough to clearly distinguish the γ and γ' peaks, and (ii) sampled more material in more orientations. Therefore, of the two data sets we believe that the HRPD data is to be preferred.

For comparison, an FEI TITAN 80/300 FEGTEM was used to determine the lattice misfit for the 2Ta alloy. Diffraction patterns were obtained from the Fast Fourier Transform of lattice images obtained using high resolution TEM, allowing a misfit of 1.2% to be determined. Clearly this was quite different from both the diffraction measurements, and, given the likely elastic constants, would imply an almost incredible level of misfit stress, even given that the interfaces are diffuse in these alloys. It is possible that localised heating by the electron beam was responsible for this discrepancy, which only serves to highlight how difficult it can be to accurately determine lattice misfit in nm-scale coherent precipitates.

Pyczak et al. [42] have previously measured the misfit in Co–9Al–9W–0.1B using a doublet fit to the {002} peak, obtaining a misfit of $+0.8\%$ at room temperature, 0.35% at 800 °C and 0.1% at 900 °C. In contrast, Sato et al. [6] measured the misfit in Co–9.2Al–9W to be 0.5%. Shinagawa et al. [43] also found that the misfit decreased with Ni content, which they attributed to Ni increasing the solubility of W in the γ; extrapolating their data to the Ni-free case implies a misfit for γ–γ' Co–Al–W two phase binary alloys of $\sim0.5\%$. These data serve to emphasise that $\sim0.2\%$ variation in misfit values between different studies is typical, with laboratory XRD measurements giving lower misfit values than higher resolution techniques based on doublet fitting. This reinforces our preference for the HRPD data over the I12 data.

3.5. Diffraction elastic constants at room temperature and 650 °C

Lattice strains were calculated from the relative change in plane spacing for each individual peak, using $\epsilon^i_{hkl}=(d^i_{hkl}-d^i_{0,hkl})/d^i_{0,hkl}$, where d^i_{hkl} is the fitted d-spacing from each reflection in each phase i, and 0 denotes initial, unloaded lattice parameter. The diffraction

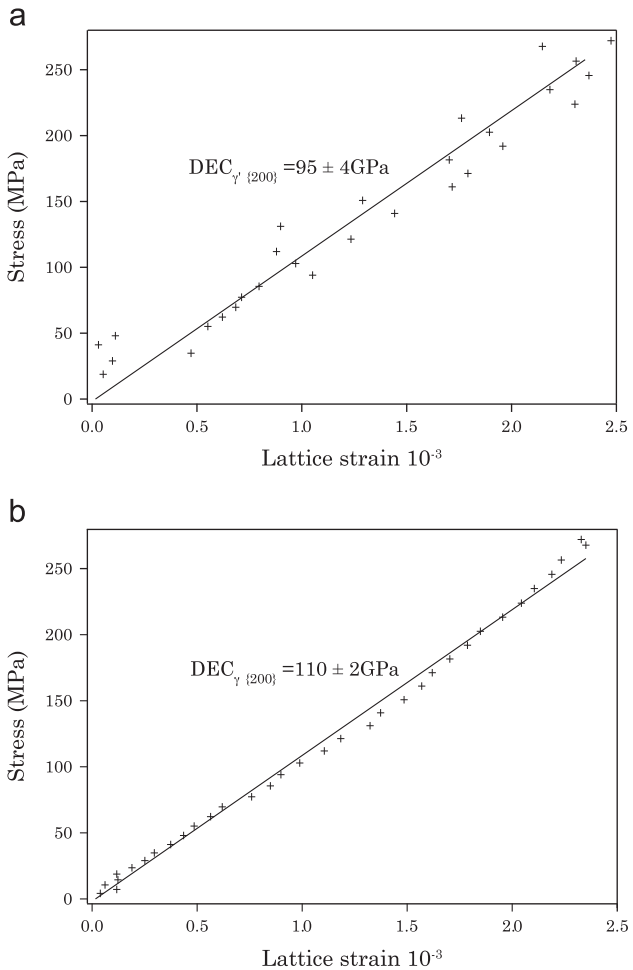

Fig. 7. Stress-lattice strain graph showing the {200} γ' and γ in the loading direction for 2Ta at room temperature in I12 experiment. The uncertainties of the γ and γ' lattice strains are estimated from Igor Pro, which are in the range of 10^{-5} to 10^{-4}.

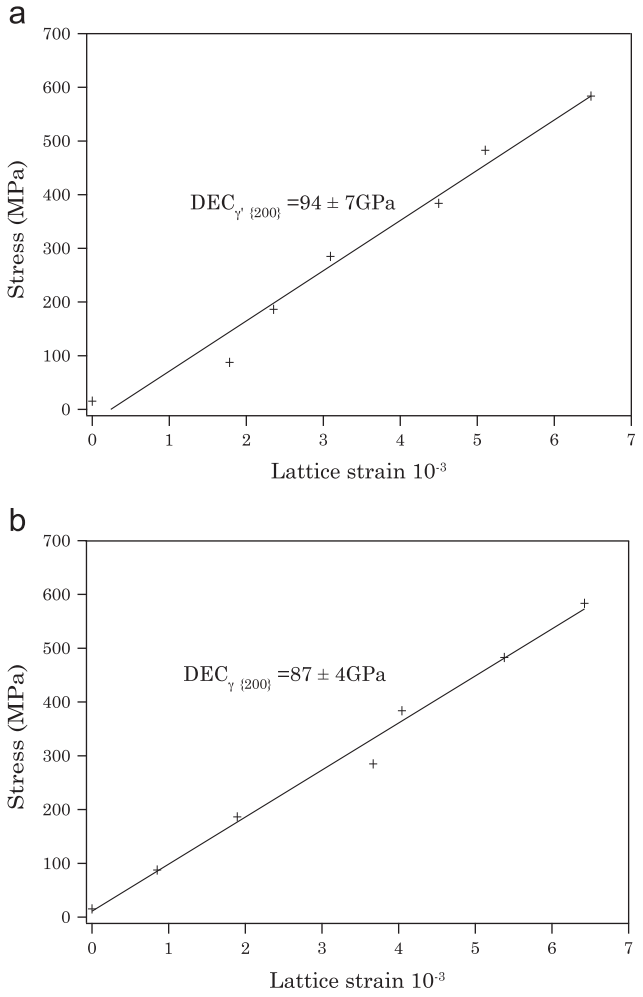

Fig. 8. Stress-lattice strain graph showing the {200} γ' and γ in the loading direction for $2Ta_{\#2}$ at room temperature in the Vulcan experiment. The uncertainties of the γ and γ' lattice strains are estimated from Igor Pro, which are in the range of 10^{-5} to 10^{-4}.

elastic constants (DECs) for each lattice plane were then determined from the gradient of the stress vs. lattice strain. It should be appreciated that the DECs are both texture and grain neighbourhood weighted. Hence, the anisotropy of the DECs is less than that of the isolated single crystal elastic constants (SECs). Given sufficient effort, the SECs can be recovered by modelling [19].

Fig. 7 is an example of stress-lattice strain graph for synchrotron diffraction data, the figure shows the {200} γ' and γ in the loading direction for 2Ta alloy at room temperature. Here the γ' lattice parameters have been determined from the {100} peak, constraining the γ/γ' {200} doublet fit. Therefore, the scatter in the γ measurements is always greater than for the γ'. It is found that the DEC for the γ' is smaller than the γ, which means the γ is stiffer than the γ' at room temperature.

For comparison, the behaviour of the 2Ta alloy (batch 2) measured using the Vulcan neutron diffractometer is provided in Fig. 8. It is possible to fit Voigt doublets to the combined {111} and {200} reflections without the need to refer to the superlattice peaks. However, there are fewer measurement points due to the reduced flux and limited beam time available. Combined with the lower resolution, this means that the fitted DECs will be less reliable (around twice the uncertainty in the linear fit). The two techniques give the same DEC for the {200} γ' stiffness, 95 GPa, but the γ results were not in agreement.

Table 3 provides the measured DECs in the 2Ta alloy at RT and 650 °C. The SECs vary linearly with the cubic anisotropy parameter,

Table 3
Constrained Diffraction Elastic Constants (DECs) (GPa) in the single, double and combined peaks, measured by synchrotron diffraction. Data for CM247LC from [17] is provided for comparison. $A_{hkl} = (h^2k^2 + h^2l^2 + k^2l^2)/(h^2 + k^2 + l^2)^2$.

$3A_{hkl}$	Plane *hkl*	Phase *x*	2Ta (RT)	2Ta (650 °C)	2Ti (RT)	2Ti (650 °C)	CM247LC (RT)
0	100	γ'	95 ± 4	118 ± 8	102 ± 8	148 ± 10	179 ± 6
0.48	210	γ'	153 ± 15	107 ± 12			214 ± 7
0.75	211	γ'	207 ± 14	146 ± 8			235 ± 9
0.75	110	γ'	146 ± 16	117 ± 20			255 ± 9
0	200	γ	110 ± 2	112 ± 1	132 ± 2	138 ± 1	157 ± 15
0.75	220	γ	184 ± 4	145 ± 8			231 ± 10
0	200	$\gamma + \gamma'$	112 ± 2	116 ± 1	130 ± 1	137 ± 1	173 ± 4
0.75	220	$\gamma + \gamma'$	193 ± 3	164 ± 3	221 ± 3	173 ± 2	247 ± 3
1	111	$\gamma + \gamma'$	186 ± 2	185 ± 2	308 ± 5	185 ± 2	276 ± 3

A_{hkl}, although in a textured sample this may not be true of the DECs. Nevertheless, the general trend observed is that the stiffness of the {100} is the lowest, as with Ni base superalloys.

Tanaka et al. [20] have measured the ratio $E_{111}/E_{100} = 385/137 = 2.8$ in liquid helium, as compared to $Ni_3(Al,Ta)$ for which values of $315/117 = 2.7$ were found. Therefore, at the cryogenic temperatures that provide the best comparison to density functional calculations, $Co_3(Al,W)$ is both about 20% stiffer and 3% more anisotropic in tension than Ni_3Al. Despite having a similar polycrystalline average Young's modulus (209 GPa) to Ni, FCC Co is much more anisotropic than Ni. Using the data quoted by Fisher and Dever [44] at room temperature of $C_{11} = 323$ GPa, $C_{12} = 102$ GPa, and $C_{44} = 66$ GPa, the Kroner DECs [45] for a texture-free polycrystal in the {111}, {110} and {100} directions would be 195, 205 and 242 GPa, respectively.

With the two phases in the system having a cube-cube orientation, the apparent directional moduli measured by diffraction for each phase will be modified due to the requirement for strain compatibility, tending towards an average between the two. In addition, there will be load shedding between grains in different orientations. Thus, lower levels of anisotropy are measured in practice than would be observed in the isolated single crystals.

Therefore, the γ' seems to be less stiff at room temperature than at 0 K, and much less stiff than Ni_3Al. In particular, the {100} DEC measured for both the 2Ti and 2Ta alloys is quite low. Unlike in the Ni superalloy system, where at room and service temperatures the γ' is the stiffer phase, the γ' is the more compliant phase in Co superalloys. Thus, load will be shed in operating conditions onto the γ, which is undesired. However, as with Ni base superalloys, the difference in moduli between the two phases is reduced at elevated temperatures more typical of gas turbine operation. Again, in common with Ni superalloys, the anisotropy of the γ' moduli was generally found to decrease with temperature.

4. Conclusions

The misfit and diffraction elastic constants in rolled polycrystalline Co–7Al–5W–2Ta and Co–6Al–6W–2Ti (at.%) have been measured using synchrotron X-ray diffraction at I12, Diamond as well as by neutron diffraction at HRPD, ISIS and Vulcan at SNS. It is found that, in these closely misfitting alloys, accurate determination of the lattice parameters is assisted by a resolution that permits the FCC peaks to be observed directly for each phase, rather than relying on constraining the position of the FCC γ' peak position from the corresponding superlattice peak and then fitting a closely overlapped doublet.

Lattice misfit values for the -2Ta and -2Ti alloys were found to be around +0.67 and +0.59%, respectively, using HRPD. The misfit was found to rise with temperature, as in Ni base superalloys. This implies

that the amount of coherency strengthening increases with temperature. The negatively misfitting Ni base superalloys show the opposite behaviour. In Co base superalloys, which are not expected to suffer from rapid coarsening due to the low diffusivity of W in the matrix phase, this should be a desirable feature.

The measured diffraction elastic constants show that the γ' phase is less stiff than the γ matrix in all orientations, which means that load shedding will occur to the γ phase. This is undesired.

For the development of engineering diffractometers that perform loading experiments in two phase materials where the two phases possess a close crystallographic relationship, such as martensites, shape memory alloys, superalloys and many other two phase metallic systems, it is recommended that improved resolution be provided such that closely misfitting peaks can be resolved more easily. In many cases such peaks correspond to the interface planes, which are of fundamental interest. Therefore, improvements in instrument resolution are of great importance to the study of advanced alloys.

Acknowledgements

The authors would like to acknowledge the financial support provided by Rolls-Royce plc and EPSRC (UK) under the DHPA scheme (HY) and by Grants EP/H004882/1 (DD, NGJ, JC, VAV) and EP/H500375/1 (HJS, NGJ). Useful conversations with Mark Hardy at Rolls-Royce plc. are also acknowledged, as is the provision of beamtime by STFC (UK) at Diamond and ISIS and at SNS, ORNL by the Scientific User Facilities Division, Office of Basic Energy Sciences, Department of Energy (USA).

References

[1] R. Schafrik, R. Sprague, Adv. Mater. Process 162 (2004) 29–33.
[2] R.C. Reed, The Superalloys, Fundamentals and Applications, 1st ed., Cambridge University Press, Cambridge, 2006, pp. 236–257.
[3] R.F. Decker, Strengthening mechanisms in nickel-base superalloys, in: Steel Strengthening Mechanisms Symposium, Climax Molybdenum Company, New York, 1969, pp. 147–170.
[4] T.M. Pollock, S. Tin, J. Propuls. Power 22 (2006) 361–374.
[5] P.C. Ruffles, Aeronaut. J. 107 (2003) 307–321.
[6] J. Sato, T. Omori, K. Oikawa, I. Ohnuma, R. Kainuma, K. Ishida, Science 312 (2006) 90–91.
[7] A. Suzuki, T.M. Pollock, Acta Mater. 56 (2008) 1288–1297.
[8] M. Ooshima, K. Tanaka, N.L. Okamoto, K. Kishida, H. Inui, J. Alloys Compd. 508 (2010) 71–78.
[9] K. Shinagawa, T. Omori, K. Oikawa, R. Kainuma, K. Ishida, Scr. Mater. 61 (2009) 612–615.
[10] A. Bauer, S. Neumeier, F. Pyczak, M. Goken, Scr. Mater. 63 (2010) 1197–1200.
[11] S. Miura, K. Ohkubo, T. Mohri, Mater. Trans. Japan Inst. Metals 48 (2007) 2403–2408.
[12] S. Kobayashi, Y. Tsukamoto, T. Takasugi, H. Chinen, T. Omori, K. Ishida, S. Zaefferer, Intermetallics 17 (2009) 1085–1089.
[13] S. Kobayashi, Y. Tsukamoto, T. Takasugi, Intermetallics 19 (2011) 1908–1912.
[14] S. Kobayashi, Y. Tsukamoto, T. Takasugi, Intermetallics 31 (2012) 94–98.
[15] A. Bauer, S. Neumeier, F. Pyczak, M. Goken, in: Superalloys 2012, TMS, Warrendale, PA, John Wiley & Sons, Hoboken, NJ, 2012, pp. 695–703.
[16] M.S. Titus, A. Suzuki, T.M. Pollock, in: Superalloys 2012, TMS, Warrendale, PA, John Wiley & Sons, Hoboken, NJ, 2012, pp. 823–832.
[17] J. Coakley, D. Dye, Scr. Mater. 67 (2012) 435–438.
[18] D. Dye, J. Coakley, V.A. Vorontsov, H.J. Stone, R.B. Rogge, Scr. Mater. 61 (2009) 109–112.
[19] M.R. Daymond, M. Preuss, B. Clausen, Acta Mater. 55 (2007) 3089–3102.
[20] K. Tanaka, T. Ohashi, K. Kishida, H. Inui, Appl. Phys. Lett. 91 (2007) 181907.
[21] Q. Yao, H. Xing, J. Sun, Appl. Phys. Lett. 89 (2006) 161906.
[22] Y.J. Wang, C.Y. Wang, Appl. Phys. Lett. 94 (2009) 261909.
[23] M. Chen, C.Y. Wang, J. Appl. Phys. 107 (2010) 093705.
[24] H.Y. Yan, V.A. Vorontsov, J. Coakley, N.G. Jones, H.J. Stone, D. Dye, in: Superalloys 2012, TMS, Warrendale, PA, John Wiley & Sons, Hoboken, NJ, 2012, pp. 705–714.
[25] H.Y. Yan, V.A. Vorontsov, D. Dye, Intermetallics (2013) ⟨http://dx.doi.org/10.1016/j.intermet.2013.10.022⟩.
[26] HRPD User Manual, ISIS - HRPD neutron light source, Oxfordshire UK. ⟨http://www.isis.stfc.ac.uk/instruments/hrpd/documents/hrpd-manual6735.pdf⟩.
[27] A. Hammersley, S. Svensson, A. Thompson, Nucl. Instrum. Methods A. 346 (1994) 312–321.
[28] F. Xue, M.L. Wang, Q. Feng, in: Superalloys 2012, TMS, Warrendale, PA, John Wiley & Sons, Hoboken, NJ, 2012, pp. 813–821.
[29] H.M. Rietveld, Acta Crystallogr. 22 (1966) 151–152.
[30] H.M. Rietveld, J. Appl. Cryst. 2 (1969) 65–71.
[31] A.C. Larson, R.B. Von Dreele, General Structure Analysis System (GSAS), Los Alamos National Laboratory Report LAUR 86–748, 2004.
[32] H.J. Stone, T.M. Holden, R.C. Reed, Acta Mater. 47 (1999) 4435–4448.
[33] J. Coakley, R.C. Reed, J.L.W. Warwick, K.M. Rahman, D. Dye, Acta Mater. 60 (2012) 2729–2738.
[34] U. Glatzel, A. Müller, Scr. Metall. Mater. 31 (1994) 285–290.
[35] U. Glatzel, Scr. Metall. Mater. 31 (1994) 291–296.
[36] V.A. Vorontsov, C. Shen, Y. Wang, D. Dye, C.M.F. Rae, Acta Mater. 58 (2010) 4110–4119.
[37] V.A. Vorontsov, L. Kovarik, M.J. Mills, C.M.F. Rae, Acta Mater. 60 (2012) 4866–4878.
[38] R.J. Gillespie, D.A. Humphreys, N.C. Baird, E.A. Robinson, Chemistry, Allyn & Bacon, Inc., London, 1986.
[39] W. Hume-Rothery, Atomic Theory for Students of Metallurgy. Monograph and Report Series No. 3. The Institute of Metals, 1969.
[40] S. Meher, H.Y. Yan, S. Nag, D. Dye, R. Banerjee, Scr. Mater. 67 (2012) 850–853.
[41] T. Omori, K. Oikawa, J. Sato, I. Ohnuma, U.R. Kattner, R. Kainuma, K. Ishida, Intermetallics 32 (2013) 274–283.
[42] F. Pyczak, A. Bauer, M. Goken, S. Neumeier, U. Lorenz, M. Oehring, N. Schell, A. Schreyer, A. Stark, F. Symanzik, Mater. Sci. Eng. A 571 (2013) 13–18.
[43] K. Shinagawa, T. Omori, J. Sato, K. Oikawa, I. Ohnuma, R. Kainuma, K. Ishida, Mater. Trans. Japan Inst. Metals 49 (2008) 1474–1479.
[44] E.S. Fisher, D. Dever, Trans. AIME 239 (1967) 48–57.
[45] D. Dye, H.J. Stone, R.C. Reed, Curr. Opin. Solid State Mater. Sci. 5 (2001) 31–37.